Monthly Notices
of the
ROYAL ASTRONOMICAL SOCIETY

MNRAS **493,** 6001–6010 (2020)
Advance Access publication 2020 February 27

doi:10.1093/mnras/staa584

First discovery of an ultra-cool white dwarf benchmark in common proper motion with an M dwarf

M. C. Lam [1]★ N. C. Hambly,[2]★ N. Lodieu [3,4] S. Blouin [5] E. J. Harvey [1] R. J. Smith,[1] M. C. Gálvez-Ortiz[6] and Z. H. Zhang [7]

[1]*Astrophysics Research Institute, Liverpool John Moores University, IC2, LSP, 146 Brownlow Hill, Liverpool L3 5RF, UK*
[2]*Institute for Astronomy, University of Edinburgh, Royal Observatory of Edinburgh, Blackford Hill, Edinburgh EH9 3HJ, UK*
[3]*Instituto de Astrofísica de Canarias (IAC), Calle Vía Láctea s/n, E-38200 La Laguna, Tenerife, Spain*
[4]*Departamento de Astrofísica, Universidad de La Laguna (ULL), E-38206 La Laguna, Tenerife, Spain*
[5]*Los Alamos National Laboratory, PO Box 1663, Mail Stop P365, Los Alamos, NM 87545, USA*
[6]*Suffolk University, Madrid Campus, C/Valle de la Viña 3, E-28003 Madrid, Spain*
[7]*School of Astronomy and Space Science, Key Laboratory of Ministry of Education, Nanjing University, Nanjing 210023, Jiangsu, China*

Accepted 2020 February 25. Received 2020 January 15; in original form 2019 December 11

ABSTRACT

Ultra-cool white dwarfs are among the oldest stellar remnants in the Universe. Their efficient gravitational settling and low effective temperatures are responsible for the smooth spectra they exhibit. For that reason, it is not possible to derive their radial velocities or to find the chemistry of the progenitors. The best that can be done is to infer such properties from associated sources, which are coeval. The simplest form of such a system is a common proper motion pair where one star is an evolved degenerate and the other a main-sequence star. In this work, we present the discovery of the first of such a system, the M dwarf LHS 6328 and the ultra-cool white dwarf PSO J1801+625, from the Pan-STARRS 1 3π survey and the *Gaia* Data Release 2. Follow-up spectra were collected covering a usable wavelength range of 3750–24 500 Å. Their spectra show that the white dwarf has an effective temperature of 3550 K and surface gravity of $\log g = 7.45 \pm 0.13$ or $\log g = 7.49 \pm 0.13$ for a CO or He core, respectively, when compared against synthetic spectra of ultra-cool white dwarf atmosphere models. The system has slightly subsolar metallicity with $-0.25 <$ [Fe/H] < 0.0, and a spatial velocity of $(U, V, W) = (-114.26 \pm 0.24, 222.94 \pm 0.60, 10.25 \pm 0.34)$ km s^{-1}, the first radial velocity and metallicity measurements of an ultra-cool white dwarf. This makes it the first and only benchmark of its kind to date.

Key words: binaries: visual – stars: low-mass – white dwarfs – solar neighbourhood.

1 INTRODUCTION

White dwarfs (WDs) are the final stage of stellar evolution of main-sequence (MS) stars with zero-age MS (ZAMS) mass less than 8 $M_\odot$. Since this mass range encompasses the vast majority of stars in the Galaxy, these degenerate remnants are the most common final product of stellar evolution, thus providing a good sample to study the history of stellar evolution and star formation in the Galaxy. In this state, there is little nuclear burning to replenish the energy they radiate away. As a consequence, the luminosity and temperature decrease monotonically with time. The electron degenerate nature means that a WD with a typical mass of 0.6 $M_\odot$ has a similar size to the Earth, giving rise to their high densities, low luminosities, and large surface gravities. Typically, it takes less than $\mathcal{O}(10^4)$ yr for metals to sink beneath the photosphere (Koester 2009), leaving only hydrogen and/or helium in the atmosphere. This leads to the lack of metallic features in the atmosphere. WDs with carbon and oxygen features are likely to have atypical evolutionary pathways (Kepler, Koester & Ourique 2016). The surface temperatures ($T_{\rm eff}$) are $\sim 10^5$ K among the hottest WDs and can be as cool as $\sim$3000 K at the faint end. When they cool below $\sim$5000 K, the hydrogen and helium lines in the optical also disappear, leaving a featureless spectrum.

Ultra-cool white dwarfs (UCWDs) are the population of featureless cool WDs (spectral type DC) that exhibit collisionally induced absorption (CIA) features. This effect sets in at around $T_{\rm eff} =$ 4000 K. This temperature limit changes depending on the chemistry of the atmosphere. Recent works suggest a distinction between UCWD and IR faint cool WDs (Kilic et al. 2012; Gianninas et al.

★ E-mail: mlam@roe.ac.uk (MCL); nch@roe.ac.uk (NCH)

2015). These cool and ultra-cool WDs have neutral colours and very low luminosities, so they are very hard to find and, therefore, study. Hence, they have been of interest to the science community for a number of years; however, we still know little about them. One of the keys is to better understand the structural and chemical evolution of the atmosphere as well as the core. Consequentially, they have significant impact in the understanding of the age and evolution of all Galactic components: through inversion of the colour–magnitude diagram (Vergely et al. 2002; Cignoni et al. 2006), or WD luminosity functions (Rowell 2013; Tremblay et al. 2014).

Common proper motion (CPM) binaries are gravitationally bound pairs formed when their birth cluster dissolves (Moeckel & Bate 2010; Kouwenhoven et al. 2011; Moeckel & Clarke 2011). Their wide physical separations mean that they have weak binding energy – the orbits can easily be disrupted; hence, they are assumed to be coeval and have evolved independently. A large sample of such binaries can be used to probe the Galactic gravitational potential (Chanamé & Gould 2004; Quinn & Smith 2009; Monroy-Rodríguez & Allen 2014; Correa-Otto, Calandra & Gil-Hutton 2017). CPM systems containing a WD and a burning star provide the advantage that the age of the system can be estimated from WD cooling, while the progenitor chemistry and the radial velocity of the system can be extracted from the co-moving counterpart. Various works have studied their kinematics (Silvestri et al. 2001), contribution to the dark matter of the Galaxy (Silvestri, Oswalt & Hawley 2002), stellar chronology (Monteiro et al. 2006; Fouesneau et al. 2019), the initial–final mass relation (IFMR; Catalán et al. 2008; Zhao et al. 2012; Andrews et al. 2015; El-Badry, Rix & Weisz 2018). As the final products of post-asymptotic giant branch stars, the mass distribution for WDs with companions is particularly useful to constrain wide binary orbital evolution as a function of spectral type (Silvestri et al. 2001).

In this work, we present the first glimpse of the UCWD PSO J180153.685+625419.450.[1] It is the first UCWD found in CPM with a hydrogen-burning low-mass star where the chemistry of the progenitor system can be found. Section 2 describes the identification of this CPM pair and the follow-up observation programme is described in Section 3. The analyses of the M dwarf and the UCWD are presented in Section 4. At the end, in Section 5, we discuss the possible origin of the degenerate component.

2 IDENTIFICATION OF THE CPM PAIR

From the WD catalogue, Lam et al. (2019, hereafter L19) selected large proper motion sources from the Pan-STARRS 1 3π Survey (Chambers et al. 2016; Magnier et al. 2016a, b, c; Waters et al. 2016), where there are a number of candidate UCWDs. When parallaxes from the *Gaia* DR2 (GDR2; Gaia Collaboration 2016, 2018) became available, PSO J1801+625 was immediately confirmed to have unusually low luminosity at $M_{\rm bol} > 16$ mag. A proper motion and parallax cross-match was performed and the WD was found to be in CPM with LHS 6328, a well catalogued M dwarf with a wealth of photometric information but never studied in detail given its unremarkable properties (see Fig. 1 for the false colour image from Pan-STARRS 1[2]). Further adding to the interest of this

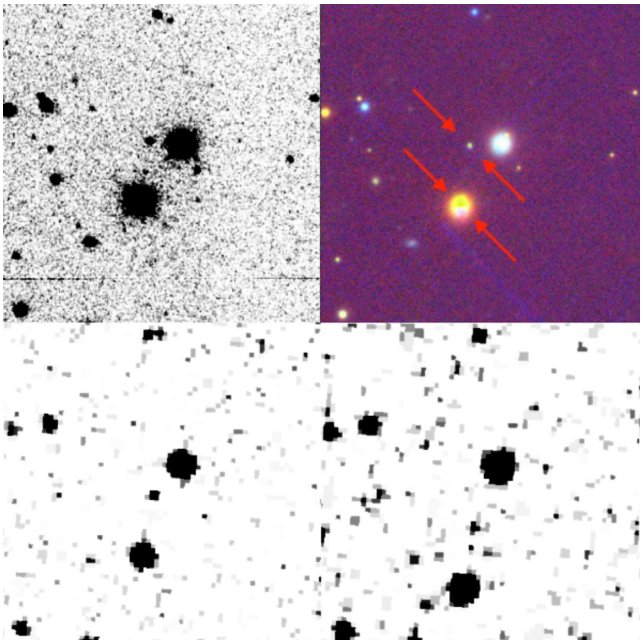

Figure 1. Clockwise from top left: LT/IO:O *r*-band image (2019); Pan-STARRS1 *g/i/y* false-colour image (2012); the First Palomar Sky Survey plate image (1952); and Guide Star Catalogue 1 plate image (1983) of the PSO J1801+625 (faint object centred at the Pan-STARRS 1 image) and LHS 6328 (bright).

system is the tangential velocity from GDR2 (corresponding to the M dwarf distance), which suggests a likely thick disc origin, $v_{\rm tan} = 4.740\,47 \times \mu \times D = 125.46\,{\rm km\,s^{-1}}$. We list the parameters of the system in Tables 1 and 2. Using photometry from Pan-STARRS 1, and the GDR2 parallax of the M dwarf, the best-fitting photometric effective temperature and atmospheric composition can be found by maximizing the extended likelihood function from L17,

$$\mathcal{L} = -\frac{1}{2}\sum_i \left\{ \left[\frac{({\rm mag}_i - {\rm DM}) - {\rm model}_i}{\sigma_i} \right]^2 + \ln\left(2\pi\sigma_i^2\right) \right\}, \quad (1)$$

where index i denotes the filter, mag is the observed magnitude, DM is the distance modulus, model is the synthetic photometry in absolute magnitude, and

$$\sigma_i^2 = \sigma_{{\rm mag},i}^2 + \left[\frac{5\log(e)}{\varpi} \right]^2 \sigma_\varpi^2 \quad (2)$$

is the combined uncertainty in magnitude $\sigma_{{\rm mag},i}$ and in parallax σ_ϖ, where ϖ is the parallax.

For the low-mass MS star, the GDR2 Apsis-Priam effective temperature is 3675 K, placing it in the range where objects are consistently overestimated (Andrae et al. 2018). The mean offset is about 300 K, thus classifying this object as an M1-M3 dwarf (Rajpurohit et al. 2013, 2018). The angular separation of the system is 21.30 arcsec; combining with the distance of the M dwarf from Bailer-Jones et al. (2018), the projected physical separation of the system is 1554.1 AU, which is a common value for CPM wide binaries (Andrews et al. 2015; El-Badry et al. 2018).

This system was not reported by a recent large-scale CPM work using the GDR2 data because of the large photometric uncertainty of the faint WD component (El-Badry et al. 2018). However, in our case, we have reliable photometry from Pan-STARRS 1 complemented with the high-quality astrometry from GDR2. With

[1]Due to its high proper motion, in Pan-STARRS DR1, this object is identified as two sources, the other source ID is PSO J180153.689+625419.758 with 19 epochs. The designation we have chosen, PSO J180153.685+625419.450, has 71 epochs of measurements.
[2]https://ps1images.stsci.edu/cgi-bin/ps1cutouts

Table 1. This table lists all the relevant archival data available in the public domain. All photometry is reported in AB magnitude except for the 2MASS magnitudes that are reported in the Vega system. [(a)]Positions are in equinox J2000.0 and epoch J2015.5 as reported in GDR2. [(b)]Distance taken from Bailer-Jones et al. (2018). [(c)]GDR2. [(d)]AAVSO Photometric All Sky Survey (APASS) (Henden et al. 2015). [(e)]Pan-STARRS 1 3π Survey. [(f)]2MASS (Skrutskie et al. 2006). [(g)]ALLWISE Data Release (Cutri et al. 2014).

Parameter	LHS 6328	PSO J1801+625
[(a)]R.A. (α)	18:01:54.228	18:01:53.691
[(a)]Dec. (δ)	+62:53:59.432	+62:54:20.414
[(a)]source_id	2159435171891858176	2159435274971074048
[(a)]μ_α/mas yr^{-1}	10.210 ± 0.046	10.498 ± 1.122
[(a)]μ_δ/mas yr^{-1}	362.712 ± 0.055	360.240 ± 0.964
[(a)]ϖ/mas	13.6769 ± 0.0258	14.7551 ± 0.5680
[(a)]ruwe	1.152	1.043
[(b)]Distance/pc	$72.962^{+0.139}_{-0.138}$	$67.737^{+2.733}_{-2.532}$
[(c)]G/mag	14.490 ± 0.0003	20.105 ± 0.007
[(c)]G_{BP}/mag	15.632 ± 0.004	20.575 ± 0.081
[(c)]G_{RP}/mag	13.430 ± 0.001	19.145 ± 0.053
[(d)]B_{APASS}/mag	17.011 ± 0.011	–
[(d)]V_{APASS}/mag	15.314 ± 0.062	–
[(e)]g_{P1}/mag	16.016 ± 0.003	21.259 ± 0.028
[(e)]r_{P1}/mag	14.769 ± 0.003	20.019 ± 0.018
[(e)]i_{P1}/mag	13.875 ± 0.007	19.517 ± 0.024
[(e)]z_{P1}/mag	13.419 ± 0.007	19.311 ± 0.035
[(e)]y_{P1}/mag	13.181 ± 0.002	19.268 ± 0.027
[(f)]J_{2MASS}/mag	12.031 ± 0.021	–
[(f)]H_{2MASS}/mag	11.508 ± 0.022	–
[(f)]K_{2MASS}/mag	11.292 ± 0.020	–
[(g)]W_1/mag	11.147 ± 0.023	–
[(g)]W_2/mag	10.979 ± 0.020	–
[(g)]W_3/mag	10.896 ± 0.051	–
[(g)]W_4/mag	>9.380	–

all of this supporting evidence, we conducted a follow-up campaign described in the following section.

3 FOLLOW-UP OBSERVATIONS

We collected additional photometric points and low-resolution spectra with the 2 m Liverpool Telescope (LT; Steele et al. 2004), the 4 m William Herschel Telescope (WHT), and the 10 m Gran Telescopio Canarias, covering a wavelength range of 3750–25 000 Å.

3.1 LT

Under the proposal JL18A03, low-resolution spectra of the UCWD and the M dwarf were collected with the SPRAT spectrograph in red-optimized mode (Piascik et al. 2014). For the UCWD, five 20 min exposures were collected on each of the dark nights on 2018 August 6 and 7; for the M dwarf, five 2 min spectra were collected on 2018 August 10.

SPRAT has a resolving power of $R \sim 300$, covering a usable wavelength range of 4000–8000 Å (blue line in Fig. 3). We re-extracted the 1D spectra from the in-house calibrated 2D spectra (LSS_NONSS of the Level 2 products). Flux calibration was done using observations of the standard Hiltner 102 taken on the same nights as the science observations. The spectra were then median averaged to give our final spectra, delivering a signal-to-noise ratio in the range of 5–10 at different wavelengths for the UCWD and about 200 for the M dwarf. Some residual telluric features could not be completely removed.

Table 2. Derived properties (apart from the distance) of the UCWD. [(a)]Using Pan-STARRS 1 photometry fitting DA and DB models with fixed $\log(g) = 8.0$ as reported in L19. [(b)]Using Pan-STARRS 1 photometry and GDR2 parallax with fitting mixed atmosphere model with fixed $\log(g) = 8.0$. [(c)]Values reported by Gentile Fusillo et al. (2019) using GDR2 photometry and parallax.

Parameter	Value
DA Photometric[(a)] $T_{\rm eff}$/K	3645^{+71}_{56}
DA Photometric[(a)] Distance/pc	$58.8^{+1.6}_{-1.3}$
DA Bolometric Magnitude[(a)]	$16.25^{+0.07}_{-0.08}$
DB Photometric[(a)] $T_{\rm eff}$/K	3158^{+25}_{-91}
DB Photometric[(a)] Distance/pc	$44.2^{+1.6}_{-2.0}$
DA Bolometric Magnitude[(a)]	$16.89^{+0.12}_{-0.10}$
Photometric[(b)] $T_{\rm eff}$/K	4264^{+7}_{-6}
Photometric[(b)] $\log(\mathcal{M}_{\rm He}/\mathcal{M}_{\rm H})$	$-1.61^{+0.07}_{-0.05}$
DA Photometric[(c)] $T_{\rm eff}$/K	3959
DA Photometric[(c)] $\log(g)$	8.045
DA Photometric[(c)] mass/M$_\odot$	0.605
DB Photometric[(c)] $T_{\rm eff}$/K	4121
DB Photometric[(c)] $\log(g)$	8.017
DB Photometric[(c)] mass/M$_\odot$	0.578

In addition to the SPRAT spectra, three 20 min medium-resolution spectra were collected with FRODOSpec at the high resolution setting ($R \sim 5300$) covering a wavelength range of 5900–8000 Å. Due to the high sensitivity of the detector, we applied cosmic ray rejection with L.A.Cosmic (van Dokkum, Bloom & Tewes 2012), before processing with the in-house automated pipeline (Barnsley, Smith & Steele 2012). The final spectrum is the weighted sum of the spectra from the 12 brightest fibres.

Additional photometric points were collected in the Sloan g, r, i, and z bands in the optical with IO:O and H band with IO:I in the near-infrared, which has a red cut-off at 17 000 Å. The H-band data were slightly affected by the saturation residual mark from the neighbouring background star. All data were collected in photometric and dark condition.

3.2 WHT

Under the service proposal SW2018A35, two half-hour science frames were collected on each night during the 2018 August 1 and 2 under bright condition with a moon phase of around 70 per cent. The spectra were collected with WHT/ISIS using the R300B and R316R blue and red gratings centred at 4499 and 8651 Å, respectively. The Intermediate-dispersion Spectrograph and Imaging System (ISIS) is a high-efficiency double-arm spectrograph with a long slit of up to 4 arcmin mounted on the WHT. The ISIS spectrograph is equipped with a blue and red detector made of 2048 × 4096 pixels whose sizes are 13.5 and 15 microns, respectively. The choice of this set-up was made to maximize the wavelength coverage, i.e. where the LT/SPRAT and WHT/ACAM do not have coverage.

Standard long-slit single object data reduction was performed using IRAF (Tody 1986, 1993). 2D spectra were median averaged separately for each night, before the two 1D spectra were optimally extracted. The final spectrum was the weighted average of the wavelength and flux-calibrated spectra using the SPECTRES

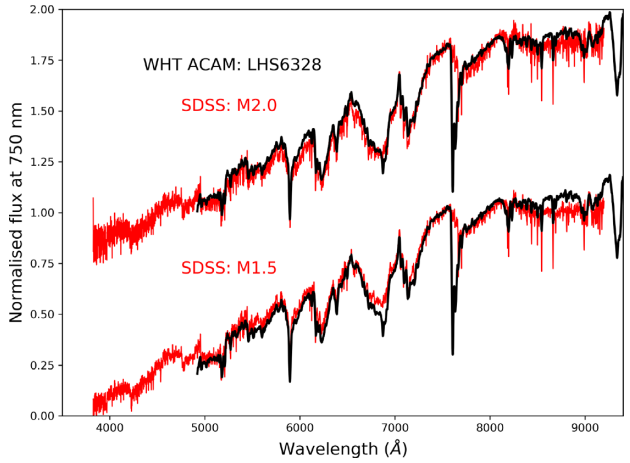

Figure 2. Template (red) fit of the ACAM spectrum (black) that gives the best-fitting solution between type M1.5 and M2 with solar metallicity. Therefore, we assign it as a type M1.75 ± 0.25 dwarf. The spectra are normalized at 7500 Å. The ACAM spectrum is not corrected for telluric absorption bands while the Sloan spectra (red) are; hence, there is a clear discrepancy at around 7600 Å due to atmospheric O_2.

package[3] (Carnall 2017). Standard observations of G93-48 were taken immediately before and after the observation on the respective nights, allowing for good removal of the telluric features, where only small residuals remain. The absolute flux calibration was done by comparing the integrated flux in the range of 4250–5250 Å between the absolute calibrated SPRAT spectrum and the ISIS blue arm. Both the red and blue ISIS spectra were then corrected by the same factor.

Three exposures of 600 s were obtained for the WD with the Auxiliary-port CAMera (ACAM) instrument mounted on the WHT on the night of 2019 July 29 between UT = 21h37 and 22h10, under the programme 095-WHT10/19A (PI: Gálvez-Ortiz; observer Lodieu). One single exposure of 300 s was collected for the M dwarf companion starting at UT = 21h27. ACAM offers low-resolution ($R \sim 400$) optical (3500–9400 Å) spectroscopy with a slit of 1 arcsec and the second-order blocking filter GG495. Arc lamps of Cu+Ne and tungsten flat-field were collected immediately after at the position of the targets. A spectroscopic standard, Ross 640 (DZA5.5; Wesemael et al. 1993), was observed at the beginning of the night to correct for the response of the detector and calibrate the flux of our target.

The data were reduced using IRAF (Tody 1986, 1993). Bias subtraction and flat-field correction were undertaken with the exposures obtained immediately following the science frames. The spectrum was extracted optimally choosing the aperture and the sky regions carefully. The spectrum of the M dwarf is shown in red in Fig. 2, while the final WHT/ACAM spectrum of the WD is displayed in green in Fig. 3.

3.3 Gran Telescopio Canarias

Photometric and spectroscopic information was obtained with the Espectrografo Multiobjeto Infra-Rojo (EMIR; Garzón et al. 2007, 2016) on the 10.4 m Gran Telescopio de Canarias (GTC) at the Observatorio del Roque de los Muchachos on the island of La Palma, under the programme GTC11-19A (PI: Lodieu). EMIR provides imaging and spectroscopic capabilities at near-infrared (0.9–2.5 microns) wavelengths. It is equipped with a 2048 × 2048 Teledyne HAWAII-2 HgCdTe detector with a pixel size of 0.2 arcsec per pixel, offering a 6.64 × 6.64 arcmin field of view.

Photometry was collected for the wide binary system on 2019 July 22 in service mode with a seeing of 0.6 arcsec, during bright time, and clear sky as part of programme GTC11_19A (PI: Lodieu). Total exposure times of 175, 175, 315, and 1743 s were set for the *Y*, *J*, *H*, and K_s passbands with on-source individual integrations of 5 s and a pattern of seven dithers to avoid saturation of the brightest stars next to the CPM pair. Spectroscopy was conducted in service mode as part of the same GTC programme with a seeing of 0.7 arcsec, bright time, and clear skies. Four and eight on-source integrations of 360 s in an ABBA pattern were collected for the WD on 2019 August 10 with the *YJ* and *HK* grisms of EMIR covering the 0.899–1.331 and 1.454–2.428 micron intervals at a spectral resolution of about 500 with a slit width of 1.0 arcsec. A spectro-photometric standard star of spectral type B9III, HIP84021 (Hube 1970), was observed immediately after the target in both the grisms.

The EMIR photometry and spectroscopy were reduced with the `pyemir` pipeline.[4] For the photometric data reduction, a median-filtered flat-field was subtracted from each individual raw image before re-projecting the images with the `reproject` utility in Python. Afterwards, the images were astrometrically calibrated with *Gaia* sources present in the EMIR field of view. The parallactic angle was set for the photometric and spectroscopic observations. 10 stars in the field were used to compute the ensemble photometry. The *H*-band photometry agrees with the independent photometry from the LT. The photometric results are listed in Table 3 in the AB magnitude system.

For the spectroscopic data reduction, the `pyemir` pipeline implements a flat-field correction, applies a wavelength calibration, and finds the offsets between the A and B positions of the spectra along the slit. The extraction of the spectra of the target and standard in each grism was conducted manually under IRAF, for selecting of the optimal apertures. The spectrum of the target was then divided by the spectrum of the standard and multiplied by a blackbody of the same temperature, smoothed to the EMIR resolution. The final spectra were down-sampled to 18.4 Å pix^{-1}, half the wavelength resolution of the optical spectra. The near-infrared spectrum of the WD is plotted in Fig. 3.

4 ANALYSIS

4.1 LHS 6328

The ACAM spectrum of the MS star was compared against the low-mass star template spectra from SDSS (Bochanski et al. 2007). Using the FRODOSpec spectra, we find that the metallicity indicators, $\zeta_{TiO/CaH}$, from Lépine, Rich & Shara (2007) and Zhang et al. (2019) are 0.92 and 0.86, respectively. Both values suggest a slightly metal-poor M dwarf. The TiO5 spectral indexes show that they are dM1.70 (Reid, Hawley & Gizis 1995), dM1.94 (Gizis 1997), and dM1.77 (Zhang et al. 2019), consistent with the best-fitting solution by eye as a type M1.75 ± 0.25 dwarf with roughly solar metallicity (Fig. 2).

[3] https://github.com/ACCarnall/spectres

[4] https://pyemir.readthedocs.io/en/latest/

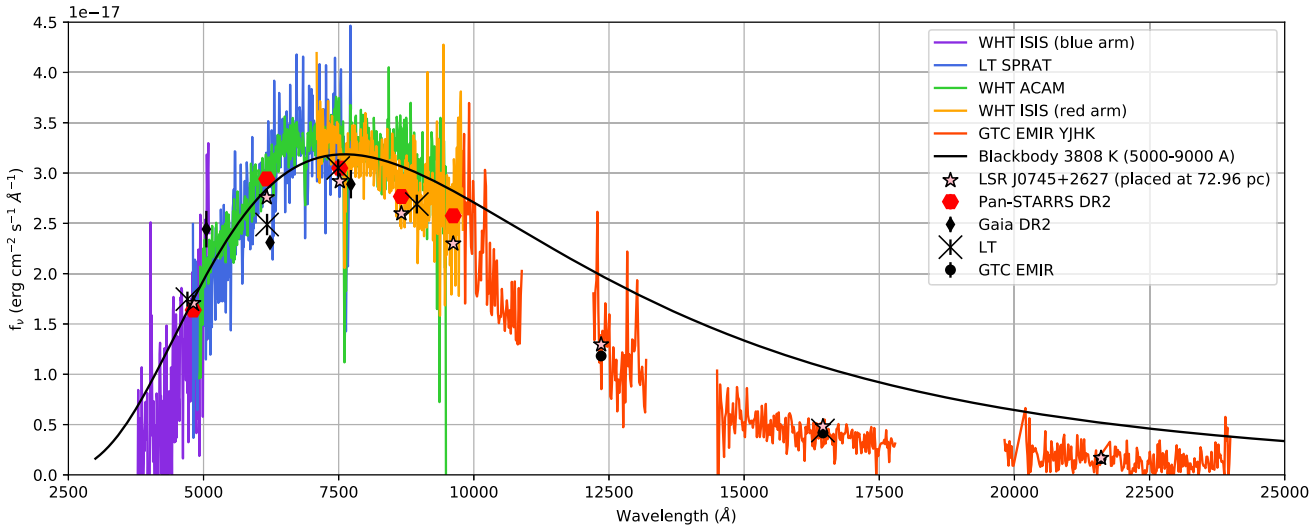

Figure 3. The spectra collected from WHT/ISIS blue and red arm (purple/orange), LT/SPRAT (blue), WHT/ACAM (green), and GTC/EMIR (red) overplotted with a blackbody spectrum at 3808 K (black, χ^2 fitted over the wavelength range of 5000–9000 Å). All optical spectra are re-sampled to 9.2 Å per pixel, while the EMIR spectra are smoothed to 18.4 Å per pixel. Only the usable ranges of the respective spectra are shown. The spectrum is smooth and does not show any absorption lines apart from the residual sky lines, consistent with the spectrum from a cool WD atmosphere. Pan-STARRS 1 *g*/*r*/*i*/*z*/*y* (left to right), *Gaia* DR2 G_{BP}/G/G_{RP}, and LT/IO:O and IO:I *g*/*r*/*i*/*z*/*H* photometry (left to right) were converted to flux using the pivot wavelengths of the respective filters. All the overlapping ranges of the spectra agree well with each other.

Table 3. Follow-up observations of the UCWD in AB magnitude.

Filter	Magnitude
g_{LT}/ mag	21.12 ± 0.07
r_{LT}/ mag	20.15 ± 0.04
i_{LT}/ mag	19.51 ± 0.03
z_{LT}/ mag	19.26 ± 0.03
J_{GTC}/ mag	19.45 ± 0.02
H_{LT}/ mag	19.90 ± 0.05
H_{GTC}/ mag	19.96 ± 0.03
K_{GTC}/ mag	20.40 ± 0.05

The radial velocity of the system was measured with eight lines that can be identified by eye from the median of the three FRODOSpec spectra, and compared against the BT-Settl[5] model atmosphere of an M dwarf at 3500 K (Allard, Homeier & Freytag 2012; Baraffe et al. 2015). The model spectrum is refraction-corrected with an air density of 0.733 amg based on the observing conditions. The median and standard deviation, computed from the product of 1.46 and the median absolute deviation (MAD), of the eight solutions, are $v_r = -1.19 \pm 0.69\,\mathrm{km\,s^{-1}}$. The full list can be found in the Appendix on Table A1. Using the AstroPy `coordinates` and `time` packages, the barycentric correction was found to be $-1.34\,\mathrm{km\,s^{-1}}$, yielding a barycentric radial velocity of $-2.53 \pm 0.69\,\mathrm{km\,s^{-1}}$. By drawing 10 000 samples from the Gaussian distributions of the proper motions, parallax, and radial velocities with their associated uncertainties as the standard deviation, the `transform_to` method gives us the Galactic velocity[6] $(U, V, W) = (-114.26 \pm 0.24, 222.94 \pm 0.60, 10.25 \pm 0.34)\,\mathrm{km\,s^{-1}}$; we use the default Solar spatial motion with the `AstroPy` package: $(U_\odot, V_\odot, W_\odot) = (11.1, 232.24, 7.25)\,\mathrm{km\,s^{-1}}$.

The absolute magnitudes of LHS 6328 in the near-infrared are consistently ∼0.8 mag fainter than the expected average value from the 8 pc sample from Table 3 of Lodieu et al. (2014). When compared with the average photometry from Pecaut & Mamajek (2013),[7] this M dwarf is also consistently fainter in the optical by the same amount. However, it is worth noting that ∼0.9 mag is within the 2 standard deviation of the sample used for averaging in Lodieu et al. (2014). This brightness also coincidentally puts it very close to the MS gap in the optical, discovered from the 100 pc sample from GDR2 (Jao et al. 2018). See more discussion in Section 5.3.

4.2 PSO J1801+625

The final calibrated spectra of the UCWD are shown in Fig. 3. The usable spectral ranges are 3750–11 000, 11 500–13 500, 14 500–18 000, and 19 500–24 000 Å. A blackbody spectrum at 3808 K is plotted as a visual reference. The combined spectrum is smooth and does not show any absorption features, which could be the case for an extreme subdwarf. The only absorption features present were identified as coming from the residual sky lines, consistent with the spectrum expected from a WD with a cool atmosphere. Catalogued photometry from Pan-STARRS 1 g_{P1}, r_{P1}, i_{P1}, and z_{P1}, GDR2 G, G_{BP}, and G_{RP}, and ensemble photometry with the field sources from the LT *g*', *r*', *i*', *z*', and H_{LT}, and from the GTC J_{EMIR}, H_{EMIR}, and K_{EMIR} photometry were converted to flux values using the respective pivot wavelengths and overplotted on to the spectra. The photometric spectral energy distribution (SED) shows a remarkable resemblance

[5] https://phoenix.ens-lyon.fr/Grids/BT-Settl

[6] Detailed descriptions can be found at https://docs.astropy.org/en/stable/api/astropy.coordinates.Galactocentric.html.

[7] http://www.pas.rochester.edu/ emamajek/EEM_dwarf_UBVIJHK_colors_Teff.txt

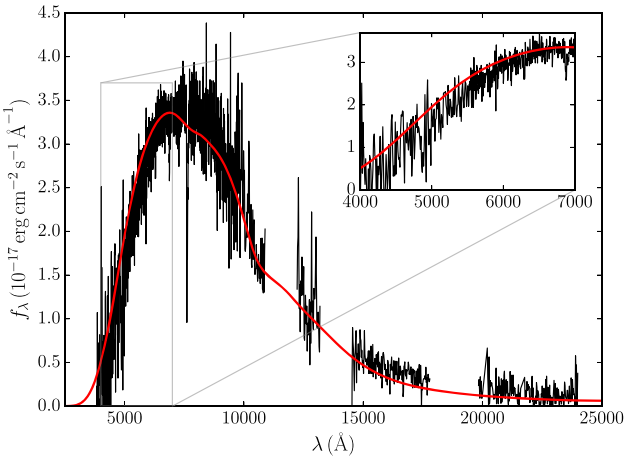

Figure 4. The best-fitting model of PSO J1801+625 indicates an effective temperature of 3550 K with low surface gravity. The best-fitting parameters are given in Table 4. The inset shows the small offset described in the text.

to that of LSR J0745+2627 if placed at the same distance (Catalán et al. 2012).

4.2.1 *Model atmosphere analysis*

We performed a fit to the available spectra of the UCWD to extract its atmospheric parameters. To do so, we used the atmosphere models described in Blouin, Dufour & Allard (2018a) and Blouin et al. (2018b). Different atmospheric compositions were tested (pure helium, pure hydrogen, and mixed compositions with H/He abundance ratios ranging from 10^{-5} to 1) and we found that the best solution is by far a pure hydrogen model. Only a pure hydrogen model can successfully reproduce both the IR flux depletion due to H_2-H_2 collision-induced absorption (CIA; Borysow, Jorgensen & Fu 2001) and the flux deficit at small wavelengths due to the far red wing of the Lyman α line broadened by collisions with H and H_2 (Kowalski & Saumon 2006). If helium is added to the model, the photospheric density becomes much higher, where H_2-He CIA dominates (Blouin, Kowalski & Dufour 2017) and the model underestimates the IR flux.

The effective temperature and the solid angle were obtained by adjusting the model fluxes to the observed spectra using a Levenberg–Marquardt algorithm. As the distance D, 72.962 pc, is known from the *Gaia* parallax, the radius R can be computed from the solid angle $\pi R^2/D^2$. Then, thanks to evolutionary models, the radius and the effective temperature can be used to obtain the mass (and $\log g$) and the cooling time of the WD. As the surface gravity resulting from this calculation was different from the one initially assumed to perform the fit, we repeated the procedure described above until the surface gravity converged.

Our best model achieves a good match to the whole SED of PSO J1801+625 as shown in Fig. 4. There seems, however, to be an offset between the model and the observations between 4000 and 6000 Å that appears to be due to an underestimation of the strength of the Lyman α broadening (see the inset of Fig. 4). The atmospheric parameters of our best-fitting model are given in Table 4. Note that the effective temperature is similar to that of LSR J0745+2627 ($T_{\rm eff} = 3880 \pm 90$ K; Catalán et al. 2012), unsurprising given the similarity between the SEDs of both objects (see Fig. 3). In Table 4, we give the mass and cooling time

Table 4. Atmospheric parameters of PSO J1801+625.

	CO core	He core
$T_{\rm eff}$ (K)	3550 ± 150	
He/H	0	
R ($R_\odot$)	0.0171 ± 0.0012	
M ($M_\odot$)	0.30 ± 0.05	0.33 ± 0.06
$\log g$	7.45 ± 0.13	7.49 ± 0.13
$\tau_{\rm cool}$ (Gyr)	5.1 ± 0.6	10.5 ± 1.5

corresponding to the case where the WD has a CO core and to the case where it has an He core (which is more appropriate given the low mass found). For the CO core case, we rely on the models of Fontaine, Brassard & Bergeron (2001) with $q({\rm He}) \equiv M_{\rm He}/M_\star = 10^{-2}$ and a thick hydrogen envelope of $M_{\rm H}/M_\star = 10^{-4}$. As for the He core case, we use the evolutionary tracks of Althaus, Serenelli & Benvenuto (2001),[8] assuming once again $M_{\rm H}/M_\star = 10^{-4}$.

5 DISCUSSION

To date, there are, including this work, 19 field UCWDs with their spectra confirmed. Their rarity and the lack of line features have made their investigation difficult at best. The lack of parallax measurements prior to GDR2 and the inhomogeneity in the sample characteristics make it difficult to do a rigorous statistical analysis. 7 of the identified UCWDs were assumed to have a typical WD surface gravity $\log g = 8.0$ (Kilic et al. 2010; Holberg et al. 2016), while the remaining 11 had the gravity fitted as a free parameter: SSSJ1556−0806 (Rowell, Kilic & Hambly 2008), J0146+1404, J1001+3903, J1238+3502, J1251+4403, J2239+0018A, J2242+0048, (Gianninas et al. 2015), LSH 3250 (Limoges, Bergeron & Lépine 2015), WD 0346+246 (Kilic et al. 2012), LHS 342, and WD 0205−053 (Blouin et al. 2019).[9] What is most surprising is how 9 of these 11 UCWDs have $\log g < 8.0$, the average mass of these being 0.36 $M_\odot$. The least massive one, J2239+0018A, has $\log g = 6.95$, corresponding to a mass of 0.2 $M_\odot$. For the two non-low-mass UCWDs, WD 0346+246 and SSSJ1556−0806, both of them have their distances underestimated as compared to the *Gaia* distance from Bailer-Jones et al. (2018). Due to the degenerate dependence on the radius and distance of the object, when an object is fitted with a distance that is too small, the radius will also be too small. Hence, these two UCWDs, having $\log g = 8.3$ and 8.0, respectively, are almost certainly going to be low mass. Though, a thorough reanalysis is necessary to perform a rigorous statistical analysis over the whole sample of UCWDs before drawing any conclusions.

We note that an overdensity of low-mass WDs is expected at low effective temperatures as the result of the slowdown in their cooling due to latent heat release from the core crystallization and the extra thermal energy resulting from the first phase of convective coupling (see fig. 15 of Bergeron et al. 2019). However, stellar evolution models show that it takes longer than the age of the Universe for an isolated star with $M < 0.45\,M_\odot$ to turn into a WD. In this sense, the 0.36 $M_\odot$ average mass for UCWDs is puzzling.

[8] http://fcaglp.fcaglp.unlp.edu.ar/ althaus/

[9] All the references here only refer to the most recently analysis that uses the most updated atmosphere models; most of them are not the original discovery articles.

5.1 Low-mass UCWD

We have arrived with a few possibilities that can be attributed to the bulk of the low-mass UCWDs in the known sample: (1) higher mass ones do not exist; (2) unaccounted input physics in the current UCWD model, supported by the poor fits found in Gianninas et al. (2015); (3) they belong to a population of WD that evolved through a specific pathway.

5.1.1 End state of single metal-rich star

There is evidence that an isolated metal-rich ($0.3 < [Fe/H] < 0.5$; Gratton et al. 2006; Origlia et al. 2006) star can lose sufficient mass to form a low-mass WD (Hansen 2005; Kalirai et al. 2007; Kilic, Stanek & Pinsonneault 2007). In order to become a UCWD, they must have cooled for a few billion years regardless of the formation scenario. It would seem rather unlikely that the majority of the 11 low-mass UCWDs have a high metallicity. Furthermore, with the current picture of metal enrichment process of the Milky Way, it is unlikely to have this many old stars with enhanced metallicity in the early time of the Galaxy.

5.1.2 Common-envelope evolution

The formation of a low-mass WD requires significant mass-loss in the post-MS stage. The current understanding is that through common-envelope (CE) evolution, the binary will produce a low-mass WD, while in a stable Roche lobe overflow system, an extremely low mass WD would be produced instead (Li et al. 2019). Post-CE systems are tight binaries (hard); dynamically hard binaries become harder (separation decreases) when interacting with a third body (known as the Heggie's Law; see Heggie 1975). If they were formed in binary systems, where is the missing companion star? Given the faintness of the UCWD, typically with $M_{bol} > 15$, any companions earlier than mid-T dwarf would have shown up in the optical and near-infrared images and/or spectra (see also the next scenario). It should be noted that given the low mass of a brown dwarf, if it should exist in the progenitor system, it could not have played a significant role in the late stage of the stellar evolution of the WD progenitor.

5.1.3 Unseen companion(s)

Using the IRSA[10] catalogue and time-series tool, ZTF DR1 (Bellm et al. 2019a, b; Graham et al. 2019) with over 50 epochs in the *g* and *r* bands, no variability is observed by either the UCWD or the M dwarf. Cross-correlations of the three up-sampled medium-resolution spectra show shifts of 0.022 pixels between the first and second epochs and −0.004 pixels between the second and third epochs. This corresponds to 0.6 and $-0.1\,km\,s^{-1}$, respectively – with signal-to-noise ratios under 0.1, such that we disregard the values. Hence, it does not support a close, unresolved companion of any significant mass. The *Ks*-band photometry reached ∼21 mag. At ∼70 pc, a mid-T dwarf should be detectable (Faherty et al. 2012; Casewell et al. 2018), which can be in the form of IR excess if they are unresolved. Similarly, if they are resolved, they would be bright enough to show up in the W2 image at 70 pc (Tinney et al. 2014).

Could they be the end products of low-mass X-ray binaries with a hidden neutron star in this system? Podsiadlowski, Rappaport & Pfahl (2001) suggest that the end products are predominantly He and low-mass hybrid HeCO WDs. When the pulsar beam is not pointing towards us, there would not be any direct detection of the neutron star. Without absorption lines with which to measure radial velocity, it is not possible to infer the presence of such a compact heavy object. Transits are not present in most binary systems, due to orbital inclination. In the stable Roche lobe overflow or double helium core WD merger formation scenario of hot subdwarf B stars, the low-mass population cannot burn helium and they eventually evolve to become helium core WDs (Han et al. 2002, 2003). This tends to produce low-mass WDs. In the case of both He and CO core WDs, this can be possible for symbiotic stellar evolution that happened at the early times of the Milky Way. HD 188112 is the prototype that bridges the late hot subdwarf B to an He core WD (Latour et al. 2016).

5.2 Typical mass UCWDs

All empirical or theoretical IFMRs (Catalán et al. 2008; Zhao et al. 2012; Andrews et al. 2015; El-Badry et al. 2018) tell the same story: *more massive stars leave behind more massive remnants*. UCWDs are old objects; they have been cooling for a few billion years. From the PARSEC stellar evolution model (Bressan et al. 2012), 1.5 and $2\,M_\odot$ solar-metallicity stars take ∼3 and ∼1.5 Gyr to become WDs, respectively. Their corresponding WD masses are $\sim 0.6\,M_\odot$, which would take ∼10 Gyr for them to cool to 3500 K, assuming a pure hydrogen atmosphere. The combined age of 11–13 Gyr would be roughly that of the thick disc and the halo. For an $\sim 0.9\,M_\odot$ WD, which would have been an $\sim 5\,M_\odot$ MS star, due to a smaller radius and low luminosity, it would take ∼11 Gyr to reach 3500 K (see fig. 12 of Bergeron et al. 2019, and note that $\sim 0.8\,M_\odot$ WD has the lowest cooling rate). More massive stars evolve quicker, so the total time required would be roughly the same as that required by WDs with typical masses.

A metal-poor star evolves faster, so it is possible for an MS star slightly under $1.5\,M_\odot$ to become WDs; however, they also have lower total mass-loss resulting in slightly more massive WDs that cool slower. Therefore, the total MS lifetime and WD cooling time for the metal-poor systems are similar to those with solar metallicity.

The seven remaining spectroscopically confirmed UCWDs in the Montreal White Dwarf Database[11] do not have the surface gravity fitted as a free parameter, so it is unclear if any of those would fit into this category of UCWDs that we can treat them as singly evolved stars.

In order for PSO J1801+625 to be a typical mass WD, it has to be ∼45 per cent closer. This requires the parallax to be 10σ off for the UCWD and a few hundreds for the equidistant M dwarf. On the other hand, if the 'low-mass UCWD' is a pair of unresolved binary UCWDs, because of the degenerate nature of WD, the more massive it is, the smaller it becomes. At a given distance and temperature, their radii are a factor of $\sqrt{2}$ smaller in order for them to have the same luminosity as a single low-mass WD. This decrease would bring the mass of the WDs up to that of a typical WD. The total lifetime of the 'unresolved binary CO-WDs' would be too long compared that expected for a CO-core WD. In any case, it does not seem probable to have all or most of the UCWDs mentioned in the previous section to be unresolved binaries with almost identical mass, radius, envelope composition, and temperature.

[10] https://irsa.ipac.caltech.edu/

[11] http://www.montrealwhitedwarfdatabase.org

5.3 What if all our measurements are outlying data points?

For a solar-metallicity single M1.75 dwarf to have the apparent magnitude as we observed, it should be at ∼110 pc. The discrepancy in the absolute magnitude of LHS 6328 and that from the averaged values of the solar neighbourhood sample is roughly 0.8 mag in all optical and near-infrared filters. NEOWISE (Wright et al. 2010; Mainzer et al. 2014) has over 1000 epochs in the *W1* and *W2* bands, where they do not show sign of variability using the periodogram tool available on their webpage. Data from the *Transiting Exoplanet Survey Satellite* (*TESS*; Ricker et al. 2015; Swade et al. 2018) were period folded with `Period04` (Lenz & Breger 2005) between 0 and 360 cycles/day in step of 0.000 625 with no 5σ peaks detected above ∼0.4 mmag.[12] Hence, neither star-spots nor occultation can be the explanation; any object that is big enough to remove 0.8 mag of light would have shown up in the spectra or photometry. If we consider any single observable to see how much it takes to compensate for the 'lost flux', it is not possible to explain the discrepancy without leading to contradicting spectral, photometric, and astrometric information. In the following, we list the possibilities to explain, if our data gathering and template fittings have been unlucky throughout, and LHS 6328 is a mild outlier.

(i) In the GDR2, LHS 6328 has an ASTROMETRIC_EXCESS_NOISE_SIG of 6.85, meaning its astrometric solution is unreliable. For the WD, it is close to the detection limit, so the parallax is also unreliable. If LHS 6328 is at the upper distance limit, 73.1 pc, it would lead to a dimming of 0.01 mag in the absolute magnitude.

(ii) The uncertainty in our M dwarf template fitting is 0.25 spectral type, while the absolute error can be as large as 0.5 spectral type, which can contribute a 0.1 mag of difference.

(iii) The metallicity indicator $\zeta_{\rm TiO/CaH}$ indicates a slightly subsolar metallicity, which puts LHS 6328 close to the border of dwarf and subdwarf. A typical subdwarf has a metallicity of [Fe/H] = −0.5; if LHS 6328 has [Fe/H] = −0.25, and combined with a shift in +0.25 spectral type (i.e. lower temperature), due to the reduced radiative pressure in the atmosphere, the radius becomes smaller by about 20 per cent (Baraffe et al. 1997; Kesseli et al. 2019). This would correspond to a change of 0.2 mag.

(iv) In the case of SDSS filters, the dispersion in the magnitudes for a given spectral type is about 0.25 mag (West, Walkowicz & Hawley 2005; Schmidt et al. 2010).

If LHS 6328 is 1.5σ from the average in all quantities, the total magnitude difference could reach 0.8 mag. This can account for the slightly spurious luminosity of a system containing two single objects at ∼70 pc, as supported by the Renormalized Unit Weight Error (RUWE; see Table 1), which are close to 1.

6 CONCLUSION

We have collected the spectra of a UCWD in CPM with a slightly metal-poor M1.75 dwarf star, LHS 6328. The UCWD has an effective temperature of 3550 K; given its low mass at 0.33 $M_\odot$, it is likely to have an He core, with a total cooling age of 10.5 ± 1.5 Gyr. This is most likely the remnant from a previously interacting binary that the companion is nowhere to be seen. This is the first system of a field UCWD with a pure hydrogen atmosphere that we can obtain the progenitor metallicity, −0.25 < [Fe/H] < 0, from its coeval MS companion. From the radial velocity measurement of the LHS 6328, we also have the first full 6D kinematics found for a UCWD, with (U, V, W) = (−114.26 ± 0.24, 222.94 ± 0.60, 10.25 ± 0.34) km s^{-1}, suggesting a thick disc-like velocity. Despite these measurements, the unclear origin of the low-mass UCWD does not allow us to confidently draw any concrete conclusions. We propose a number of explanations but there is no evidence for any of the suggested scenarios. We believe it is necessary to run simulations on a wide range of configurations in order to understand what kind of evolution scenarios could have led to a system like LHS 6328 and PSO J1801+625.

[12] *TESS* unique object ID: TIC 233068267.

ACKNOWLEDGEMENTS

ML acknowledges financial support from the OPTICON. ML thanks P. R. McWhirter for the frequency analysis on the M-dwarf variability.

NL was financially supported by the Spanish Ministry of Economy and Competitiveness (MINECO) under the grant AYA2015-69350-C3-2-P (2016-2019). NL thanks Lee Patrick, Alina Streblyanska, and the `pyemir` developers for their help during the reduction of the EMIR data.

SB acknowledges support from the Laboratory Directed Research and Development programme of Los Alamos National Laboratory under project number 20190624PRD2.

The LT is operated on the island of La Palma by Liverpool John Moores University in the Spanish Observatorio del Roque de los Muchachos of the Instituto de Astrofísica de Canarias with financial support from the UK Science and Technology Facilities Council.

The WHT and its service programme are operated on the island of La Palma by the Isaac Newton Group of Telescopes in the Spanish Observatorio del Roque de los Muchachos of the Instituto de Astrofísica de Canarias.

Based on observations made with the Gran Telescopio Canarias (GTC), installed in the Spanish Observatorio del Roque de los Muchachos of the Instituto de Astrofísica de Canarias, in the island of La Palma.

This work is partly based on data obtained with the instrument EMIR, built by a Consortium led by the Instituto de Astrofísica de Canarias. EMIR was funded by GRANTECAN and the National Plan of Astronomy and Astrophysics of the Spanish Government.

This publication makes use of data products from the Two Micron All Sky Survey, which is a joint project of the University of Massachusetts and the Infrared Processing and Analysis Center/California Institute of Technology, funded by the National Aeronautics and Space Administration and the National Science Foundation.

This publication makes use of data products from the Wide-field Infrared Survey Explorer, which is a joint project of the University of California, Los Angeles, and the Jet Propulsion Laboratory/California Institute of Technology, funded by the National Aeronautics and Space Administration.

This paper includes data collected by the *TESS* mission. Funding for the *TESS* mission is provided by the NASA Explorer Program.

The Pan-STARRS1 Surveys (PS1) and the PS1 public science archive have been made possible through contributions by the Institute for Astronomy, the University of Hawaii, the Pan-STARRS Project Office, the Max-Planck Society and its participating institutes, the Max Planck Institute for Astronomy, Heidelberg and the Max Planck Institute for Extraterrestrial Physics, Garching, The Johns Hopkins University, Durham University, the Univer-

sity of Edinburgh, the Queen's University Belfast, the Harvard-Smithsonian Center for Astrophysics, the Las Cumbres Observatory Global Telescope Network Incorporated, the National Central University of Taiwan, the Space Telescope Science Institute, the National Aeronautics and Space Administration under Grant No. NNX08AR22G issued through the Planetary Science Division of the NASA Science Mission Directorate, the National Science Foundation Grant No. AST-1238877, the University of Maryland, Eotvos Lorand University (ELTE), the Los Alamos National Laboratory, and the Gordon and Betty Moore Foundation.

This work has made use of data from the European Space Agency (ESA) mission *Gaia* (https://www.cosmos.esa.int/gaia), processed by the *Gaia* Data Processing and Analysis Consortium (DPAC; https://www.cosmos.esa.int/web/gaia/dpac/consortium). Funding for the DPAC has been provided by national institutions, in particular the institutions participating in the *Gaia* Multilateral Agreement.

REFERENCES

Allard F., Homeier D., Freytag B., 2012, Phil. Trans. R. Soc. London Ser. A, 370, 2765
Althaus L. G., Serenelli A. M., Benvenuto O. G., 2001, MNRAS, 323, 471
Andrae R. et al., 2018, A&A, 616, A8
Andrews J. J., Agüeros M. A., Gianninas A., Kilic M., Dhital S., Anderson S. F., 2015, ApJ, 815, 63
Bailer-Jones C. A. L., Rybizki J., Fouesneau M., Mantelet G., Andrae R., 2018, AJ, 156, 58
Baraffe I., Chabrier G., Allard F., Hauschildt P. H., 1997, A&A, 327, 1054
Baraffe I., Homeier D., Allard F., Chabrier G., 2015, A&A, 577, A42
Barnsley R., Smith R., Steele I., 2012, in Ballester P., Egret D., Lorente N. P. F., eds, ASP Conf. Ser. Vol. 461, Astronomical Data Analysis Software and Systems XXI. Astron. Soc. Pac., San Francisco, p. 517
Bellm E. C. et al., 2019a, PASP, 131, 018002
Bellm E. C. et al., 2019b, PASP, 131, 068003
Bergeron P., Dufour P., Fontaine G., Coutu S., Blouin S., Genest-Beaulieu C., Bédard A., Rolland B., 2019, ApJ, 876, 67
Blouin S., Kowalski P. M., Dufour P., 2017, ApJ, 848, 36
Blouin S., Dufour P., Allard N. F., 2018a, ApJ, 863, 184
Blouin S., Dufour P., Allard N. F., Kilic M., 2018b, ApJ, 867, 161
Blouin S., Dufour P., Thibeault C., Allard N. F., 2019, ApJ, 878, 63
Bochanski J. J., West A. A., Hawley S. L., Covey K. R., 2007, AJ, 133, 531
Borysow A., Jorgensen U. G., Fu Y., 2001, J. Quant. Spectrosc. Radiat. Transfer, 68, 235
Bressan A., Marigo P., Girardi L., Salasnich B., Dal Cero C., Rubele S., Nanni A., 2012, MNRAS, 427, 127
Carnall A. C., 2017, preprint (arXiv:1705.05165)
Casewell S. L., Littlefair S. P., Parsons S. G., Marsh T. R., Fortney J. J., Marley M. S., 2018, MNRAS, 481, 5216
Catalán S., Isern J., García-Berro E., Ribas I., Allende Prieto C., Bonanos A. Z., 2008, A&A, 477, 213
Catalán S. et al., 2012, A&A, 546, L3
Chambers K. C. et al., 2016, preprint (arXiv:1612.05560)
Chanamé J., Gould A., 2004, ApJ, 601, 289
Cignoni M., Degl'Innocenti S., Prada Moroni P. G., Shore S. N., 2006, A&A, 459, 783
Correa-Otto J. A., Calandra M. F., Gil-Hutton R. A., 2017, A&A, 600, A59
Cutri R. M. et al., 2014, VizieR Online Data Catalog. p. II/328
El-Badry K., Rix H.-W., Weisz D. R., 2018, ApJ, 860, L17
Faherty J. K. et al., 2012, ApJ, 752, 56
Fontaine G., Brassard P., Bergeron P., 2001, PASP, 113, 409
Fouesneau M., Rix H.-W., von Hippel T., Hogg D. W., Tian H., 2019, ApJ, 870, 9
Gaia Collaboration, 2016, A&A, 595, A1
Gaia Collaboration, 2018, A&A, 616, A1
Garzón F. et al., 2007, in Guzmán R., ed., Rev. Mex. Astron. Astrofis. Conf. Ser. Vol. 29, First Light Science with the GTC. Instituto de Astronomía, Mexico, p. 12
Garzón F. et al., 2016, in Christopher J. E., Luc S., Hideki T., eds, Proc. SPIE Conf. Ser. Vol. 9908, Ground-Based and Airborne Instrumentation for Astronomy VI. SPIE, Bellingham, p. 99081J
Gentile Fusillo N. P. et al., 2019, MNRAS, 482, 4570
Gianninas A., Curd B., Thorstensen J. R., Kilic M., Bergeron P., Andrews J. J., Canton P., Agüeros M. A., 2015, MNRAS, 449, 3966
Gizis J. E., 1997, AJ, 113, 806
Graham M. J. et al., 2019, PASP, 131, 078001
Gratton R., Bragaglia A., Carretta E., Tosi M., 2006, ApJ, 642, 462
Han Z., Podsiadlowski P., Maxted P. F. L., Marsh T. R., Ivanova N., 2002, MNRAS, 336, 449
Han Z., Podsiadlowski P., Maxted P. F. L., Marsh T. R., 2003, MNRAS, 341, 669
Hansen B. M. S., 2005, ApJ, 635, 522
Heggie D. C., 1975, MNRAS, 173, 729
Henden A. A., Levine S., Terrell D., Welch D. L., 2015, Am. Astron. Soc. Meeting Abstr., 225, 336.16
Holberg J. B., Oswalt T. D., Sion E. M., McCook G. P., 2016, MNRAS, 462, 2295
Hube D. P., 1970, Mem. R. Astron. Soc., 72, 233
Jao W.-C., Henry T. J., Gies D. R., Hambly N. C., 2018, ApJ, 861, L11
Kalirai J. S., Bergeron P., Hansen B. M. S., Kelson D. D., Reitzel D. B., Rich R. M., Richer H. B., 2007, ApJ, 671, 748
Kepler S. O., Koester D., Ourique G., 2016, Science, 352, 67
Kesseli A. Y. et al., 2019, AJ, 157, 63
Kilic M., Stanek K. Z., Pinsonneault M. H., 2007, ApJ, 671, 761
Kilic M. et al., 2010, ApJS, 190, 77
Kilic M., Thorstensen J. R., Kowalski P. M., Andrews J., 2012, MNRAS, 423, L132
Koester D., 2009, A&A, 498, 517
Kouwenhoven M. B. N., Goodwin S. P., Davies M. B., Parker R. J., Kroupa P., Malmberg D., 2011, in Qain S., Leung K., Zhu L., Kwok S., eds, ASP Conf. Ser. Vol. 451, 9th Pacific Rim Conference on Stellar Astrophysics (The Origin of Very Wide Binary Stars). Astron. Soc. Pac., San Francisco, p. 9
Kowalski P. M., Saumon D., 2006, ApJ, 651, L137
Lam M. C. et al., 2019, MNRAS, 482, 715 (L19)
Latour M. et al., 2016, A&A, 585, A115
Lenz P., Breger M., 2005, Commun. Asteroseismology, 146, 53
Lépine S., Rich R. M., Shara M. M., 2007, ApJ, 669, 1235
Li Z., Chen X., Chen H.-L., Han Z., 2019, ApJ, 871, 148
Limoges M. M., Bergeron P., Lépine S., 2015, ApJS, 219, 19
Lodieu N., Pérez-Garrido A., Béjar V. J. S., Gauza B., Ruiz M. T., Rebolo R., Pinfield D. J., Martín E. L., 2014, A&A, 569, A120
Magnier E. A. et al., 2016a, preprint (arXiv:1612.05240)
Magnier E. A. et al., 2016b, preprint (arXiv:1612.05242)
Magnier E. A. et al., 2016c, preprint (arXiv:1612.05244)
Mainzer A. K. et al., 2014, Am. Astron. Soc. Meeting Abstr., 223, 217.08
Moeckel N., Bate M. R., 2010, MNRAS, 404, 721
Moeckel N., Clarke C. J., 2011, MNRAS, 415, 1179
Monroy-Rodríguez M. A., Allen C., 2014, ApJ, 790, 159
Monteiro H., Jao W.-C., Henry T., Subasavage J., Beaulieu T., 2006, ApJ, 638, 446
Origlia L., Valenti E., Rich R. M., Ferraro F. R., 2006, ApJ, 646, 499
Pecaut M. J., Mamajek E. E., 2013, ApJS, 208, 9
Piascik A. S., Steele I. A., Bates S. D., Mottram C. J., Smith R. J., Barnsley R. M., Bolton B., 2014, in Suzanne K. R., Ian S. M., Hideki T., eds, Proc. SPIE Conf. Ser. Vol. 9147, Ground-Based and Airborne Instrumentation for Astronomy V. SPIE, Bellingham, p. 91478H
Podsiadlowski P., Rappaport S., Pfahl E., 2001, in Vanbeveren D., ed., Astrophysics and Space Science Library, Vol. 264, The Influence of Binaries on Stellar Population Studies. Springer-Verlag, Berlin, p. 355
Quinn D. P., Smith M. C., 2009, MNRAS, 400, 2128
Rajpurohit A. S., Reylé C., Allard F., Homeier D., Schultheis M., Bessell M. S., Robin A. C., 2013, A&A, 556, A15

Rajpurohit A. S., Allard F., Teixeira G. D. C., Homeier D., Rajpurohit S., Mousis O., 2018, A&A, 610, A19
Reid I. N., Hawley S. L., Gizis J. E., 1995, AJ, 110, 1838
Ricker G. R. et al., 2015, J. Astron. Telesc. Instrum. Syst., 1, 014003
Rowell N., 2013, MNRAS, 434, 1549
Rowell N. R., Kilic M., Hambly N. C., 2008, MNRAS, 385, L23
Schmidt S. J., West A. A., Hawley S. L., Pineda J. S., 2010, AJ, 139, 1808
Silvestri N. M., Oswalt T. D., Wood M. A., Smith J. A., Reid I. N., Sion E. M., 2001, AJ, 121, 503
Silvestri N. M., Oswalt T. D., Hawley S. L., 2002, AJ, 124, 1118
Skrutskie M. F. et al., 2006, AJ, 131, 1163
Steele I. A. et al., 2004, in Oschmann Jacobus M. J., ed., Proc. SPIE Conf. Ser. Vol. 5489, Ground-Based Telescopes. SPIE, Bellingham, p. 679
Swade D., Fleming S., Jenkins J. M., Latham D. W., Morgan E., Mullally S. E., Sparks W., Vanderspek R., 2018, in Alison B. P., Robert L. S., Chris R. B., eds, Proc. SPIE Conf. Ser. Vol. 10704, Observatory Operations: Strategies, Processes, and Systems VII. SPIE, Bellingham, p. 1070415
Tinney C. G., Faherty J. K., Kirkpatrick J. D., Cushing M., Morley C. V., Wright E. L., 2014, ApJ, 796, 39
Tody D., 1986, Proc. SPIE, IN: Instrumentation in astronomy VI; Society of Photo-Optical Instrumentation Engineers. SPIE, Bellingham, p. 733
Tody D., 1993, in Hanisch R. J., Brissenden R. J. V., Barnes J., eds, ASP Conf. Ser. Vol. 52, Astronomical Data Analysis Software and Systems II. Astron. Soc. Pac., San Francisco, p. 173
Tremblay P. E., Kalirai J. S., Soderblom D. R., Cignoni M., Cummings J., 2014, ApJ, 791, 92
van Dokkum P. G., Bloom J., Tewes M., 2012, L.A.Cosmic: Laplacian Cosmic Ray Identification, Astrophysics Source Code Library, record ascl:1207.005
Vergely J. L., Köppen J., Egret D., Bienaymé O., 2002, A&A, 390, 917
Waters C. Z. et al., 2016, preprint (arXiv:1612.05245)
Wesemael F., Greenstein J. L., Liebert J., Lamontagne R., Fontaine G., Bergeron P., Glaspey J. W., 1993, PASP, 105, 761
West A. A., Walkowicz L. M., Hawley S. L., 2005, PASP, 117, 706
Wright E. L. et al., 2010, AJ, 140, 1868
Zhang S. et al., 2019, ApJS, 240, 31
Zhao J. K., Oswalt T. D., Willson L. A., Wang Q., Zhao G., 2012, ApJ, 746, 144

APPENDIX

The eight lines used for computing the radial velocity of the M dwarf are listed in Table A1. The spectrum used for the measurement is the median of the three 20 min FRODOSpec spectra.

Table A1. The wavelengths of the model absorption lines from BT-SETTL are corrected with an air density of 0.733 amg based on the observing conditions. The eight lines that can be identified by eyes are used to compute the radial velocities.

BT-SETTL/Å	Measured/Å	Radial velocity/km s^{-1}
6122.68	6122.5	−0.88
6162.63	6162.5	−0.63
6450.30	6449.9	−1.86
6463.06	6463.0	−0.28
7326.70	7326.4	−1.23
7511.59	7511.3	−1.16
7665.50	7665.1	−1.57
7699.56	7699.0	−2.18

This paper has been typeset from a TEX/LATEX file prepared by the author.